Construction and Building Materials 466 (2025) 140214

Contents lists available at ScienceDirect

Construction and Building Materials

journal homepage: www.elsevier.com/locate/conbuildmat

Deep learning-based prediction of particle size distributions in construction and demolition waste recycling using convolutional neural networks on 3D laser triangulation data

Nils Kroell [a,b,*], Eric Thor [a], Lieve Göbbels [a], Paula Schönfelder [a], Xiaozheng Chen [a,b]

[a] Department of Anthropogenic Material Cycles, RWTH Aachen University, Wuellnerstr. 2, Aachen D-52062, Germany
[b] STADLER Anlagenbau GmbH, Max-Planck-Straße 21, Altshausen D-88361, Germany

ARTICLE INFO

Keywords:
Machine learning
Deep learning
Inline sensor-based material flow characterization
Circular economy
Sieve analysis
Recycled concrete aggregates
Explainable artificial intelligence (XAI)

ABSTRACT

To enhance sustainability in the construction industry, substituting primary with recycled aggregates from construction and demolition waste (CDW) is essential. However, the necessary quality assessment of recycled aggregates, especially their particle size distribution (PSD), through sampling and manual sieving is time-consuming and prone to sampling errors due to the heterogeneity of CDW waste and fluctuating material flows combined with small sampling and manual sieving volumes. Here, we introduce a novel inline monitoring approach using convolutional neural networks (CNNs) to estimate PSDs from inline 3D laser triangulation (3DLT) sensor data of both primary and recycled aggregate particles. Analyzing 174,220 particles across nine size classes with a dual camera 3DLT sensor, a customized VGG-inspired CNN model outperformed other architectures, achieving accuracies of 80.8 % and 75.0 % for primary and recycled aggregates at particle level, respectively. Most errors were near-miss classifications, yielding a mean absolute error of 1.0 vol% in PSD predictions at material flow level. Explainable artificial intelligence techniques confirmed the reliance of CNNs on particle contours for robust classification. Our findings offer a pathway for inline PSD monitoring in processing of both primary and recycled aggregates, contributing to a more quality-orientated, circular, and sustainable construction industry.

1. Introduction

The construction industry is one of the most resource-intensive sectors [7]. The German construction industry consumed about 584.6 Mt/a of aggregate materials in 2020 alone [1], resulting in significant environmental impacts [12,34,35,3]. With an increasing number of buildings nearing the end of their life, a crucial strategy to minimize these environmental impacts is the substitution of primary aggregates with recycled (RC) aggregates from construction and demolition waste (CDW) resulting in significant environmental benefits such as greenhouse gas emission and energy savings as well as the conservation of natural resources and habitats [34,38,3].

However, RC construction materials currently account for merely 13.2 wt% of the aggregate demand in Germany [1]. Moreover, with 56.4 Mt/a (73.3 wt%) of the total usage, their utilization is predominantly limited to underground engineering applications. While the capacity for uptake in underground engineering projects is anticipated to decrease due to fewer new road alignments [24], an increasing demand is projected in building construction applications [33]. Increasing the substitution of primary aggregates with RC aggregates, especially in building construction applications, is therefore a crucial measure to reduce the environmental impacts of the construction industry and meet sustainability targets (e.g., [2,8,6,43,41,42]).

The process of turning CDW into recycled aggregates generally involves multiple stages carried out by mobile processing plants, leading to a variety of procedures being applied in practice, depending on the plant used. However, the overarching steps are largely the same: First, the CDW material is reduced to smaller sizes ("crushing"). Second,

Abbreviations: 3DLT, 3D laser triangulation; BGR, Blue-green-red; CDW, Construction and demolition waste; CNN, Convolutional neural network; Grad-CAM, Gradient-weighted class activation mapping; PRIM, Primary material; PSD, Particle size distribution; RC, Recycled; RCM, Recycled material; RGB, Red-green-blue; XAI, Explainable artificial intelligence.

* Correspondence to: STADLER Anlagenbau GmbH, Max-Planck-Str. 2, Altshausen D-88361, Germany.
E-mail address: nils.kroell@w-stadler.de (N. Kroell).

https://doi.org/10.1016/j.conbuildmat.2025.140214
Received 20 October 2024; Received in revised form 21 January 2025; Accepted 26 January 2025
Available online 8 February 2025

loosened foreign material, such as reinforcement steel or plastic films, are removed by magnetic or air separators, depending on the type of foreign material ("sorting"). Third, the material flow is sieved into one or multiple particle size classes that meet the desired particle size requirements ("sieving"). Material that does not meet the requirements, i.e., oversized particles, are recirculated into the processing stream for further crushing [45]. The so produced recycled aggregates can then be utilized to substitute primary aggregates in new construction processes.

To substitute these primary aggregates, especially in applications with high quality demands such as building construction, RC materials must meet defined quality standards (e.g., [9,20,19]). A crucial quality requirement for RC aggregates is the *particle size distribution (PSD)*, defined in ISO 20290-5:2023 [21], which is currently determined through sampling and manual sieve analyses [21].

Sampling and manual sieve analyses are time-consuming, costly, and often limited in their informational value (depending on the representativeness of the sample) [22,32]. Furthermore, the obtained PSDs are typically obtained with a significant time delay [32], which hinders the ability to promptly react to quality changes or adjust processing parameters based on fluctuating material flow characteristics [27]. Moreover, the high personnel costs of manual PSD determinations result in infrequently conducted quality control checks [29]. Combined with high plant throughputs and fluctuating material flow characteristics, this leads to a limited information value of the results, intransparency along the value chain [29] and a limited acceptance of the produced RC aggregates [16].

1.1. Sensor-based determination of particle size distributions

A solution to these problems could lie in a near real-time determination of PSDs using inline sensor technology and involves a three-stage characterization process: First, 3D laser triangulation (3DLT) sensors could monitor the material flow inline on conveyor belts after its processing into RC aggregates. Second, the recorded 3DLT data could be segmented into individual particles using (deep-learning-based) instance segmentation. Third, the particle size of each particle could be predicted using machine/deep learning models and lastly be aggregated to a PSDs.

The inline determined PSD could then first be used to monitor and document the achieved PSD as a crucial quality criterion in near real time. If a deviation from the targeted PSD is identified, process parameters, such as the rotation speed of comminution machines, could be adapted to produce a RC aggregate with a consistent PSD despite fluctuating material flow characteristics in the infeed material flow. If such an inline PSD monitoring system could be developed, this could help to (i) document existing RC qualities (PSDs) to strengthen the acceptance of RC aggregates, and (ii) improve RC qualities due to dynamically adapted process parameters.

A particular challenge in predicting PSDs of RC aggregates is the fact that particle sizes in CDW recycling according to ISO 20290-5:2023 [21] are not defined by geometric particle dimensions, but by the result of the sieving process, i.e., the mesh size of a sieve through which the particle can still barely pass. Thus, particle sizes and PSDs cannot be geometrically measured but require being *predicted*, for instance using machine learning [32].

1.2. Related work

Sensor-based prediction of PSDs has already been investigated for primary raw materials [13,14,18,25,40,48], commercial waste [22], and alternative fuels [4]. For CDW, however, previous studies have been limited to prediction from 2D stockpile images [3].

In previous work, we have demonstrated that it is both technically feasible to segment CDW particles based on 3DLT data using deep learning-based instance segmentation [46] and that particle sizes can be predicted from segmented/singled CDW particles using particle geometries [26] and machine learning models [32].

1.3. Aim and research questions

This paper substantially extends our previous efforts. Instead of relying on a fixed and human-made extraction of geometric features from the 3DLT data, we aim at training a convolutional neural network (CNN) end-to-end that predicts the particle sizes directly from the segmented 3DLT data. The aim of the present paper is thus to investigate if it is possible to train a CNN that can extract meaningful features directly from the given 3DLT image of CDW particles and accurately predict particle size classes and PSDs. To achieve this research aim, we intend to answer the following three research questions:

- **RQ 1:** How accurately can particle sizes according to [21] of primary and RC aggregates be predicted using CNNs and 3D laser triangulation data and which CNN architectures are suitable for the particle size prediction task?
- **RQ 2:** How can explainable AI techniques be used to better understand the model behaviour and which input features influence the classification result?
- **RQ 3:** How accurately can PSDs be determined, if the CNN predictions are aggregated at a material flow level?

2. Material and methods

2.1. Materials

For answering the aforementioned research questions, two datasets containing 3DLT recordings of singled out particles and their corresponding particle sizes according to [21] were created. The dataset *PRIM* contains images of primary aggregates to be able to compare our results with previous studies on primary aggregates (cf. Section 1.2). The dataset *RCM* contains images of RC aggregates to be able to evaluate the influence of more complex particle shapes of RC aggregates.

2.1.1. PRIM

For primary aggregates, virgin quartz stones (Min2C quartz pebbles light; particle size ranges 2 mm – 8 mm, 8 mm – 16 mm, and 16 mm – 32 mm; Min2C GmbH [A-3390 Melk, Austria]) were chosen due to their hardness and relatively regular shape. As shown in Fig. 1a and Fig. 2a, the PRIM particles were characterized by a uniform, bright surface, and predominantly smooth and round surface texture.

2.1.2. RCM

The RC aggregates (particle size range 0 mm – 45 mm) originated from a CDW processing plant in Germany (MAV Krefeld GmbH [47809 Krefeld, Germany]), mainly consisting of minerals, building stone, pottery (pieces of tiles), concrete and brick debris (cf. Fig. 1b, Fig. 2b). These aggregates are currently used, for, e.g., frost protection layers or gravel bearing layers according to TL SoB-StB 20 [10] or TL Gestein-StB 04/23 [11] [46]. The obtained samples were dried at 85°C until weight consistency and then sieved into defined particle size classes (cf. Section 2.2).

2.2. Sample preparation

Both PRIM and RCM samples were sieved according to [21] on the analytical sieve machine from Siebtechnik GmbH (Mühlheim [Ruhr], Germany) with the screen mesh sizes 3.15 mm, 4.0 mm, 5.0 mm, 6.3 mm, 8.0 mm, 10.0 mm, 12.5 mm, 16.0 mmm, 22.4 mm, and 31.5 mm. The sieving duration was set to 90 seconds at a frequency of 1,400 rpm.

After sieving, the PRIM samples were cleaned with water and dried at 85 °C until weight consistency to reduce the dust formation at the data acquisition stage (cf. Section 2.3). The RCM samples were not cleaned to

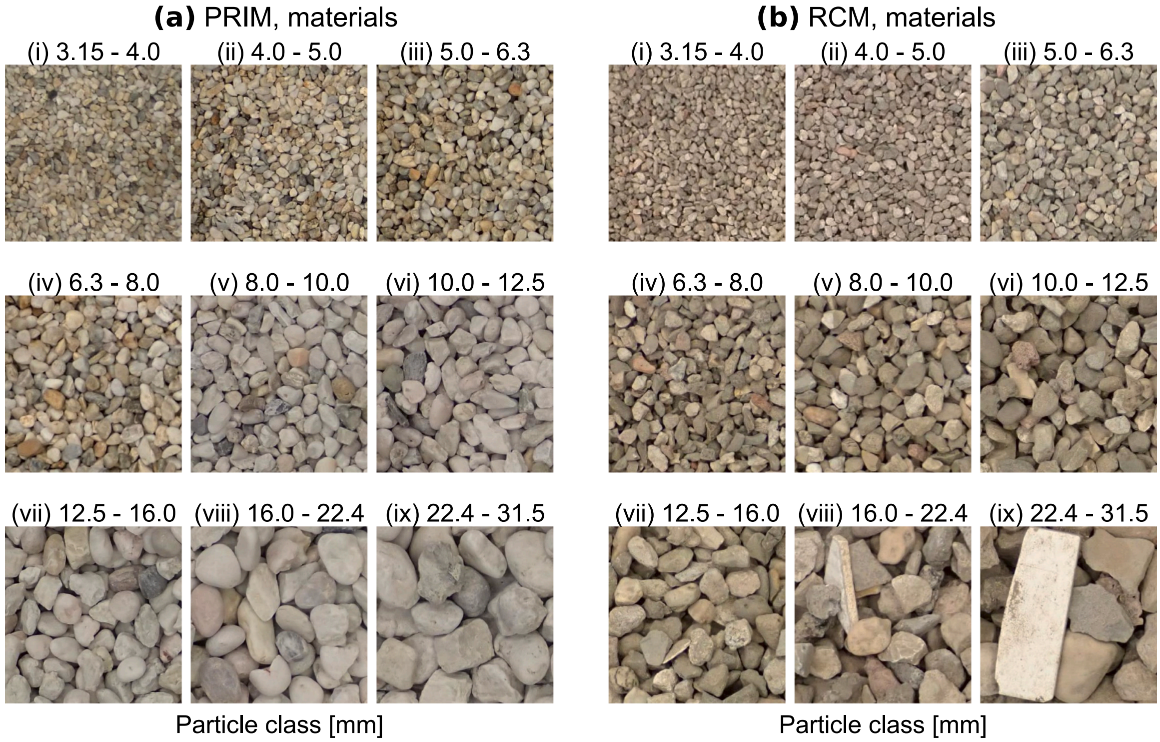

Fig. 1. RGB images of (a) PRIM and (b) RCM particles in the nine investigated material classes.

simulate realistic recording conditions in a CDW processing plant. The CDW samples included 0.56 wt% non-target materials (e.g., glass, wood, plastics), which were manually sorted out, as this investigation focused on the particle size prediction for RC aggregates and because their mass shares were low.

2.3. Data acquisition

The sieved and prepared samples were then recorded using a custom-made dual camera-3DLT setup (Fig. S1 in Supplementary Materials). The 3DLT setup used the combination of a vibrating conveyor and a black conveyor belt (belt speed: 0.15 m/s, effective belt width: 385 mm) to present the material flow as a monolayer with separate, non-occluding particles to the 3DLT sensor (singled material flow presentation). The 3DLT sensor consisted of two line-lasers (Z-Laser Z120M18-F-660-Ip45; 120 mW output; 660 nm laser wavelength; Z-LASER GmbH [79100 Freiberg, Germany]), a custom-made mirror setup, and a AT C3–1280-CL 3DLT camera (AT – Automation Technology GmbH [23843 Bad Oldesloe, Germany]) resulting in a dual camera-3DLT setup. After image acquisition, the front and back images from the mirror setup were processed and calibrated using a custom-developed, 3DLT calibration software in Python, resulting in 3DLT recordings with a spatial resolution of 0.758 mm/Pixel in the z-direction (height) and 0.331 mm/Pixel in the x- and y-direction (width and length). The preconditioned and sieved samples from Section 2.2 were sequentially placed on the 3DLT-setup, such that the particle size classes of each recording were known. Table 1 summarizes the number of images (i.e., particles) recorded within each particle size class for the PRIM and RCM dataset.

2.4. Image preprocessing

After calibration, the individual particles in the 3DLT recordings were automatically extracted using standard image processing techniques (*skimage.measure.label()* [44]) and then further pre-processed for the respective CNN models.

2.4.1. Image size alignment

Since the used CNN models require the same input image size for each particle, a data preprocessing step was necessary to (i) ensure uniform image size for all particles and (ii) retain particle size information for the CNNs. Rather than scaling all images based on the largest particle, potentially losing information in smaller size classes, the 99.5th percentile of maximum bounding box dimensions of all particles was used as a reference (PRIM: 107 px [35.4 mm], RCM: 119 px [39.4 mm]). Images of particles smaller than this reference were padded with black pixels (representing a height of 0 mm) to obtain square images with the reference dimensions. 0.5 % of the particles in the dataset have a bounding box that is larger than the reference size and are therefore centrally cropped to the reference size. After the image size alignment, images were scaled to a final size of 224 px $\times$ 224 px (hereinafter referred to as 224 px image size) or 64 px $\times$ 64 px (hereinafter referred to as 64 px image size) depending on the used CNN model (see Section 2.5). For models requiring RGB-shaped input instead of grayscale data, the grayscale channel was replicated three times to create RGB-equivalent input data.

2.4.2. Gray value scaling

After 3DLT calibration (see Section 2.3), each gray value corresponds to a height of 1 mm. Due to the investigated particle size range (3.15 mm – 31.5 mm, cf. Section 2.2), this does not utilize the full range (0–255) of an 8-bit grayscale image. To standardize brightness values, particularly for transfer learning CNN models, all images were subsequently scaled based on the largest gray value per dataset to obtain a grayscale range of 0–255.

2.5. Model training

2.5.1. Investigated CNN architectures

Different CNN architectures with increasing model complexity were trained and evaluated for predicting the particle size class of each particle based on the preprocessed 3DLT image (cf. Section 2.4). The first three models (CNN architectures B, D, and F) proposed by [31] are

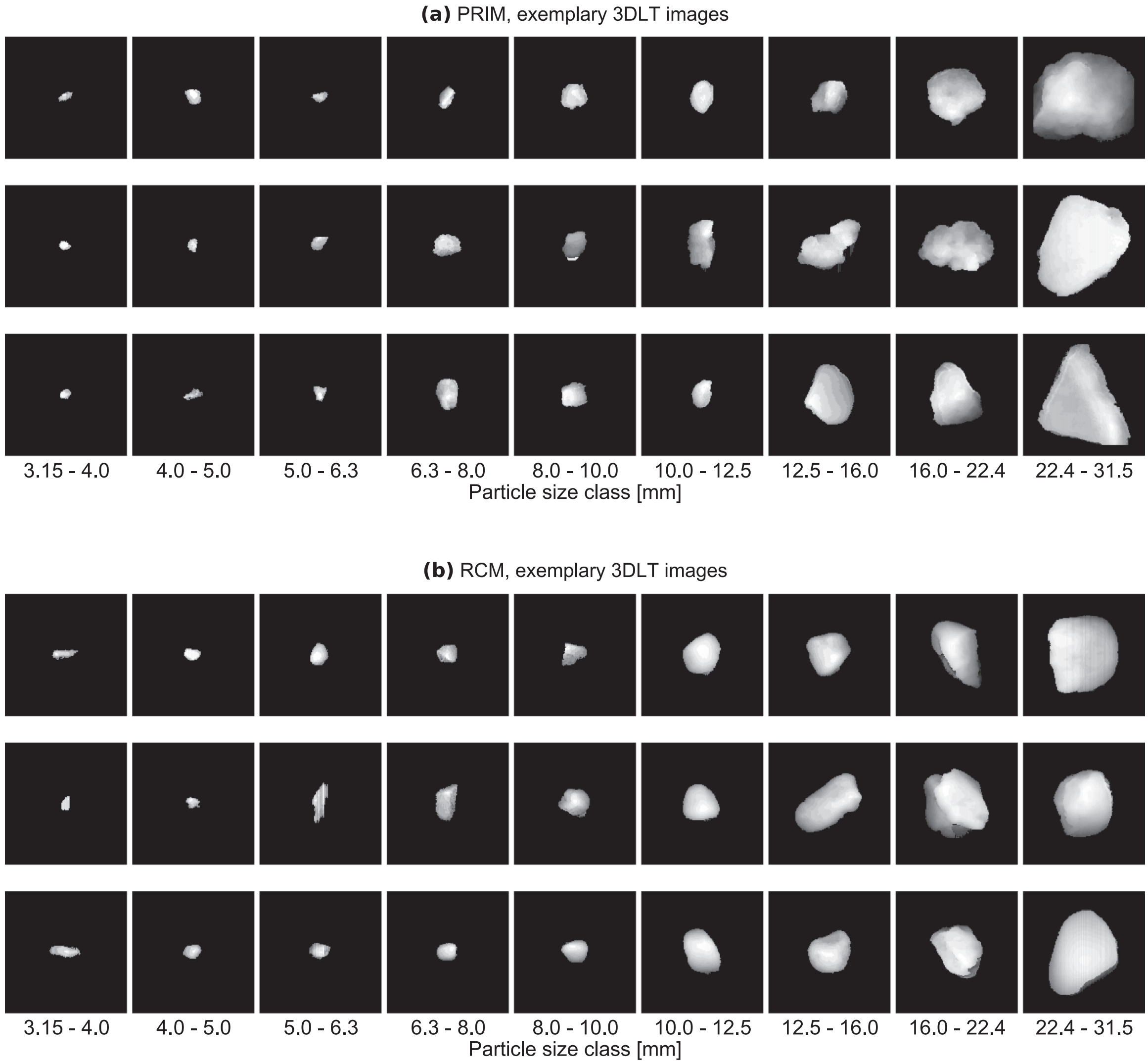

Fig. 2. Exemplary, randomly selected 3DLT images of the nine investigated particle size classes for the (a) PRIM and (b) RCM dataset.

Table 1
Overview of #images per particle size class in the PRIM and RCM dataset.

Particle in class [mm]	#Images	
	PRIM	RCM
3.15 – 4	10,911	3,750
4 – 5	21,209	15,066
5 – 6.3	24,412	33,656
6.3 – 8	19,863	14,129
8 – 10.0	8,056	3,143
10 – 12.5	5,591	2,260
12.5 – 16	3,492	1,194
16 – 22.4	2,209	3,494
22.4 – 31.5	1,085	700
$\sum$	96,828	77,392

simplified versions of the VGG architecture and were trained from scratch. For transfer learning, the CNN architectures VGG16 [39], VGG19 [39], ResNet50 [15], and DenseNet [17] were trained using transfer learning (see Table S1 in Supplementary Materials).

2.5.2. *Training and optimization*

2.5.2.1. Train-validation-test-split. Both datasets were randomly split into a training-validation dataset for model training and hyperparameter optimization (80 %) and an independent test dataset (20 %) to evaluate the final model performance. For hyperparameter optimization, the training-validation dataset was split into 80 % training and 20 % validation data. To monitor the model performance per epoch on out-of-sample data and to create a validation curve, in each epoch, 20 % of the training data have been extracted for the calculation of the respective out-of-sample error. After training, the out-of-sample error is estimated using the validation data.

2.5.2.2. Hyperparameter optimization. For hyperparameter optimization, pre-tests we conducted have shown that the learning rate λ and the input image size have the strongest influence on the model training. To meet computational constraints in model training, we therefore decided to focus the hyperparameter optimization on the hyperparameters (i) learning rate and (ii) input image size. The learning rate was varied $\lambda \in \{10^{-4}, 10^{-3}, 10^{-2}\}$, which was chosen based on previous research results. The input image size was identified was varied to be between 64 px and 224 px for the transfer learning models. All non-transfer learning models were trained on a constant input image size of 64 px due to the lower number of model parameters.

2.5.2.3. Training procedure. All CNNs were trained with a fixed batch size of 256 instances for a maximum of 30 epochs. For the transfer learning models (VGG16, VGG19, ResNet, and DenseNet), we applied their respective preprocessing functions, which convert the data from RGB (red-green-blue) to BGR (blue-green-red) and zero-center their values.

All CNNs were trained using the Adam optimizer [23] and a sparse categorical cross-entropy loss function. We used the callback *early_stop_monitor*, which stops the training after no improvement in the validation error is observed for 4 epochs [36] and the callback *learning_rate_reducer* to reduce the learning rate of the model after 2 epochs of no improvement on the out of sample error, to close in on the optimum and prevent oscillation [47].

2.6. Model evaluation

2.6.1. Metrics

The final models were evaluated both at the particle level (Section 2.6.1.1) and material flow level (Section 2.6.1.2).

2.6.1.1. Evaluation at particle level. On a particle level, predicting particle size classes represents a classification problem. Thus, we assessed the model quality at a particle level primarily using the accuracy (Eq. (1)) and confusion matrices. Accuracy refers to the proportion of particles for which the particle size class has been correctly predicted. The confusion matrix, on the other hand, compares the predicted particle size class against the actual particle size class for each prediction done on the test or validation set. Here, correct predictions are presented on the antidiagonal (i.e., bottom left to top right) of the confusion matrix.

$$\text{accuracy} = \frac{\#\text{correct classified particles}}{\#\text{all particles}} \quad (1)$$

2.6.1.2. Aggregation and evaluation at material flow level. Besides a correct classification of the particle level, the alignment of the predicted PSD (resulting from aggregating particle classifications) with the actual PSD (resulting from sieve analysis of a sample) is especially important.

Assuming equal densities for particles in PRIM and RCM datasets, the mass-based PSD defined in [21] matches a volume-based PSD. Since particle volumes can be measured using 3DLT [30,32], they are available for each particle in the PRIM and RCM datasets. Using the true or predicted particle size class per particle and the resulting true 3DLT particle volume (V_j) and predicted 3DLT particle volume ($\widehat{V}_j$), a true ($PSD_V(i)$) and predicted ($\widehat{PSD}_V(i)$) volume-based particle size distribution can be calculated according to Eqs. (2) and (3).

$$PSD_V(i) = \frac{1}{V_{total}} \sum_{j=1}^{c_i} V_j \quad (2)$$

$$\widehat{PSD}_V(i) = \frac{1}{V_{total}} \sum_{j=1}^{c_i} \widehat{V}_j \quad (3)$$

The prediction of the PSD is a regression problem. We therefore used the mean absolute error (*MAE*, Eq. (4)) to assess the extent to which the true PSD and predicted PSD match.

$$MAE = \frac{1}{n} \sum_{i=1}^{n} \left| PSD_V(i) - \widehat{PSD}_V(i) \right| \quad (4)$$

As the calculation of the MAE depends on the considered PSD, we use the lower and upper bounds and a mean PSD for frost protection layers and gravel bearing layers 0 mm – 45 mm according to TL SoB-StB 20 [10] as a reference, since this is the current quality standard for the investigated RC aggregates. As our investigation focuses on the particle size range 3.15 mm to 31.5 mm and used different screen mesh sizes, we linearly interpolated the PSD requirements from TL SoB-StB 20, to obtain three reference PSDs (min, mean, max) that correspond to the PSD requirements from TL SoB-StB 20 as shown in Table S2 in the Supplementary Materials.

2.6.2. Explainable AI

Besides merely focusing on creating models with the best possible performance, our focus has also been on creating more explainable models to be able to better investigate their robustness and limitations. For instance, class maps are used to investigate the performance and prediction uncertainty in combination with the difficulty of the respective predictions. Moreover, to investigate what parts of the image are most influential to the decision made by the model, heat maps of the feature activations have been created. By using these explainable AI (XAI) tools, it is then possible to draw more in-depth conclusions of the actual performance and robustness of the models, thereby allowing for more accurate suggestions for further optimization.

2.6.2.1. Feature activations. For visualizing the feature activations, we used the gradient-weighted class activation mapping (Grad-CAM) [37]. Grad-CAM elucidates the regions within an input image that significantly influence the classification decision of a network regarding a specific class. One of the key strengths of Grad-CAM lies in its ability to provide interpretability without compromising model accuracy, thereby retaining the original architecture of deep models. By leveraging the gradients flowing into the final convolutional layer of the CNN, Grad-CAM generates a heat map that highlights the crucial regions of an image. This heat map is constructed by computing the gradient of the predicted class score with respect to the feature maps of the last convolutional layer, thereby discerning the significance of each feature map for a specific class.

2.6.2.2. Class maps. Class maps have been made to acquire insights on the model performance in such a way that model uncertainty and performance can be compared with the difficulty of the individual observations. To do so, observations were color coded based on the class assigned by the model (i.e., the prediction). To determine the model uncertainty, the probability of an observation belonging to another class is extracted. Additionally, observation difficulty is defined by localized farness, where the nearest neighbors are calculated using the kernel density tree, a *k*-NN algorithm designed for fast conversion of *N*-point problems. Here, Euclidean distance is used as the distance metric and the Epanechnikov kernel is used as a weighting function to weigh the local distances and calculate the corresponding class probability, defined by $P(i \in g_i)$ [5]. What follows is the actual calculation of localized farness, using the following formula:

$$\text{localized farness} = 1.0 - P(i \in g_i) \quad (5)$$

This allows a comparison of the observation difficulty in terms of similarity with other observations in the same class: if an observation is highly similar, the localized farness will approach zero, while high dissimilarity leads to near-one values. In the remainder of this work, localized farness will be referred to as *farness*.

3. Results and discussion

Based on the developed methodology and created datasets, Sections 3.1, 3.2, and 3.3 aim at answering the research questions RQ 1, RQ 2, and RQ 3 (cf. Section 1.3), respectively.

3.1. Prediction of particle sizes (RQ 1)

Table 2 summarizes the achieved training and validation accuracies for all investigated CNNs on the (a) PRIM and (b) RCM dataset for all investigated hyperparameters. The highest validation accuracy – which represents the CNN with the best hyperparameter setting for the given task and the investigated hyperparameter settings – for each model is boldfaced, while the overall best model is boldfaced and underlined.

Table 2
Training and validation accuracy for the seven investigated CNN architectures on the (a) PRIM and (b) RCM dataset for all investigated hyperparameter settings. Highest validation accuracy per model highlighted in bold, highest validation accuracy over all models highlighted in bold and underlined.

(a)	Learning rate	10^{-4}		10^{-3}		10^{-2}	
	Model/input size	**64 px**	**224 px**	**64 px**	**224 px**	**64 px**	**224 px**
Train	B	68.1 %	-	71.8 %	-	63.8 %	-
	D	82.3 %	-	86.2 %	-	73.4 %	-
	F	84.3 %	-	86.9 %	-	71.8 %	-
	VGG−16	78.8 %	85.1 %	78.9 %	83.8 %	54.9 %	80.9 %
	VGG−19	79.7 %	84.8 %	43.4 %	84.0 %	43.4 %	74.4 %
	ResNet	80.9 %	69.0 %	79.9 %	76.7 %	80.4 %	57.7 %
	DenseNet	74.8 %	49.5 %	74.1 %	66.1 %	74.2 %	43.4 %
Val	B	70.0 %	-	**73.6 %**	-	59.4 %	-
	D	**80.4 %**	-	79.6 %	-	73.5 %	-
	F	**80.8 %**	-	79.5 %	-	72.2 %	-
	VGG−16	77.9 %	**79.1 %**	76.6 %	78.7 %	50.6 %	77.3 %
	VGG−19	78.1 %	**78.7 %**	43.4 %	78.5 %	43.4 %	73.2 %
	ResNet	76.7 %	68.9 %	**76.9 %**	75.4 %	76.4 %	56.1 %
	DenseNet	**74.5 %**	50.1 %	74.2 %	68.0 %	74.3 %	43.4 %
(b)	**Learning rate**	10^{-4}		10^{-3}		10^{-2}	
	Model/input size	**64 px**	**224 px**	**64 px**	**224 px**	**64 px**	**224 px**
Train	B	65.1 %	-	67.5 %	-	65.6 %	-
	D	77.5 %	-	80.2 %	-	58.7 %	-
	F	82.9 %	-	78.1 %	-	55.8 %	-
	VGG−16	74.6 %	79.7 %	73.4 %	77.1 %	25.3 %	74.5 %
	VGG−19	75.3 %	78.1 %	73.4 %	76.6 %	25.3 %	71.7 %
	ResNet	77.7 %	57.2 %	76.8 %	72.7 %	75.1 %	48.3 %
	DenseNet	69.4 %	48.6 %	70.4 %	54.1 %	70.2 %	65.0 %
Val	B	67.4 %	-	**69.3 %**	-	67.0 %	-
	D	**74.3 %**	-	73.2 %	-	61.3 %	-
	F	**75.0 %**	-	73.7 %	-	59.5 %	-
	VGG−16	73.1 %	**73.7 %**	72.7 %	72.8 %	25.0 %	72.0 %
	VGG−19	**73.8 %**	72.6 %	72.9 %	72.5 %	25.0 %	69.9 %
	ResNet	72.3 %	56.7 %	**72.6 %**	70.2 %	72.2 %	48.3 %
	DenseNet	69.8 %	49.4 %	70.3 %	55.1 %	**70.8 %**	66.4 %

3.1.1. Influence of input image size

Regarding the input image size, the investigated CNNs do not benefit from an increased image size, as across all models trained on 64 px and 224 px data, no significant difference between the classification accuracies based on 64 px and 224 px input images is found ($p = 0.895$[4]), cf. Table 2. Subsequent comparisons therefore focus on the 64 px input image size models.

This finding may thus indicate that an input image size of 64 px is sufficient for the model to obtain the differences between the investigated particle size classes, or at least the advantages of an increased input image size do not outweigh the disadvantages of a higher overfitting probability.

3.1.2. Influence of learning rate

When comparing the influence of the initial learning rate across all 64 px models (Table 2), the learning rate significantly influences model performance ($p = 0.002$[5]). Across all models and datasets, lower learning rates result in improved classification results. For example, when calculating the arithmetic mean over all models and datasets for 64 px images, the validation accuracy increases from 59.3 % at $\lambda = 10^{-2}$, over 72.0 % at $\lambda = 10^{-3}$ to 74.6 % at $\lambda = 10^{-4}$.

3.1.3. Influence of CNN architectures

When comparing the model architectures based on the optimal image size and learning rate (cf. bold numbers in Table 2), it can be seen that the classification accuracy first increases and then decreases with increasing model complexity between CNN B (73.6 % for PRIM & 69.3 % for RCM), CNN D (80.4 % & 74.3 %), CNN F (80.8 % & 75.0 %), VGG16 (79.1 % & 73.7 %), VGG 19 (78.7 % & 73.8 %), ResNet (76.9 % & 72.6 %) to DenseNet (74.5 % & 70.8 %), cf. Fig. 3 h. For both datasets, the CNN F architectures achieves the highest classification accuracy, thus indicating a potential optimal model complexity for the investigated datasets and given prediction task.

3.1.4. Influence material origin (PRIM vs. RCM)

Comparing both datasets PRIM and RCM shows that all models achieve on average + 4.9 percentage points more accurate predictions (validation set) on the PRIM dataset (mean accuracy: 77.7 %, top accuracy: 80.8 %) compared to the RCM dataset (mean accuracy: 72.8 %, top accuracy: 75.0 %). A plausible reason for this observation is the less regular particle shapes of RCM compared to PRIM, as shown in Fig. 1 and Fig. 2.

3.1.5. Learning curves

Fig. 3 supports these findings and gives further insight into the training process by visualizing the model-specific learning curves. For all models, a rapid decrease of the training and validation loss at the beginning of the training process is observed before the loss reaches a plateau at the end of the training process and the learning rate reduction and early stopping callbacks are activated. Comparing the CNN architectures trained from scratch (CNNs B, D, F) with the transfer learning models (VGG16, VGG19, ResNet, and DenseNet), the positive effects of transfer learning are confirmed, as the models start at a lower initial loss. As shown before, the loss of CNNs on the PRIM dataset is lower compared to RCM dataset. For all models, a slight overfitting is observed at the end of the training processes (training loss decreases while the validation loss plateaus), indicating that a further training of the CNNs would not further increase the model's accuracy.

3.1.6. Confusion matrix

In Fig. 4, confusion matrices of the top 3-performing models for the PRIM and RCM datasets are shown, to allow for a more detailed

[4] *p*-values express the level of significance. Here, we calculated the *p*-value based on a dependent *t*-test for paired samples using *scipy.stats.ttest_rel()*

[5] Calculated based on one-way ANOVA test using *scipy.stats.f_oneway()*

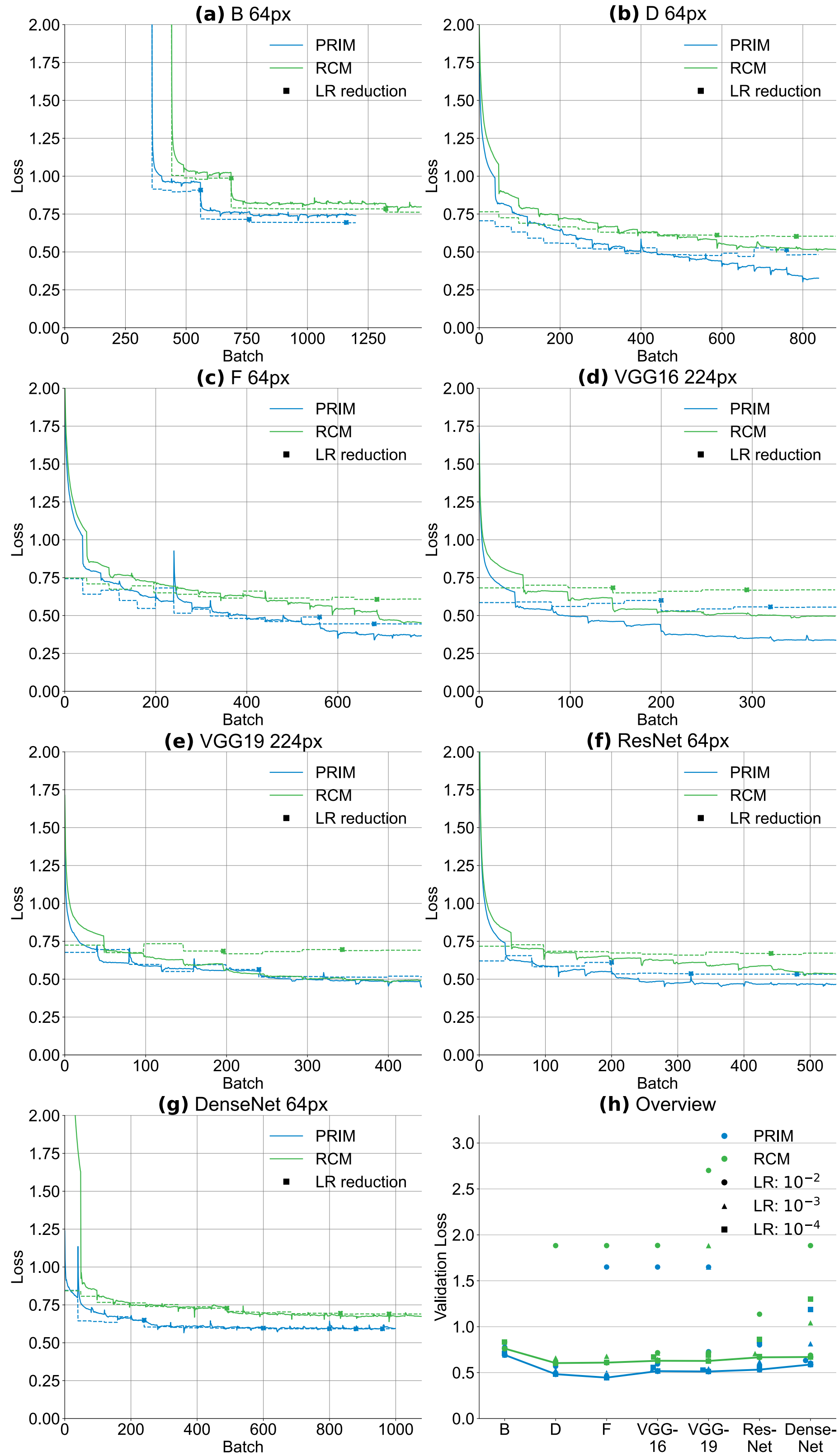

Fig. 3. Batch-wise overview on the training process of the investigated CNN architectures (best performing configuration per architecture); continued lines: training loss, dashed lines: validation loss.

performance comparison. For all models, a similar trend can be observed. That is, all three models predict the true particle size class within ± one particle size class deviation in more than 98 % of all cases and the true particle size class ± two particle size classes deviation in 100 % of all cases.

Further, the confusion matrices show that predictions are generally more accurate for the higher particle size classes compared to the lower ones, despite a higher number of particles in the latter class during

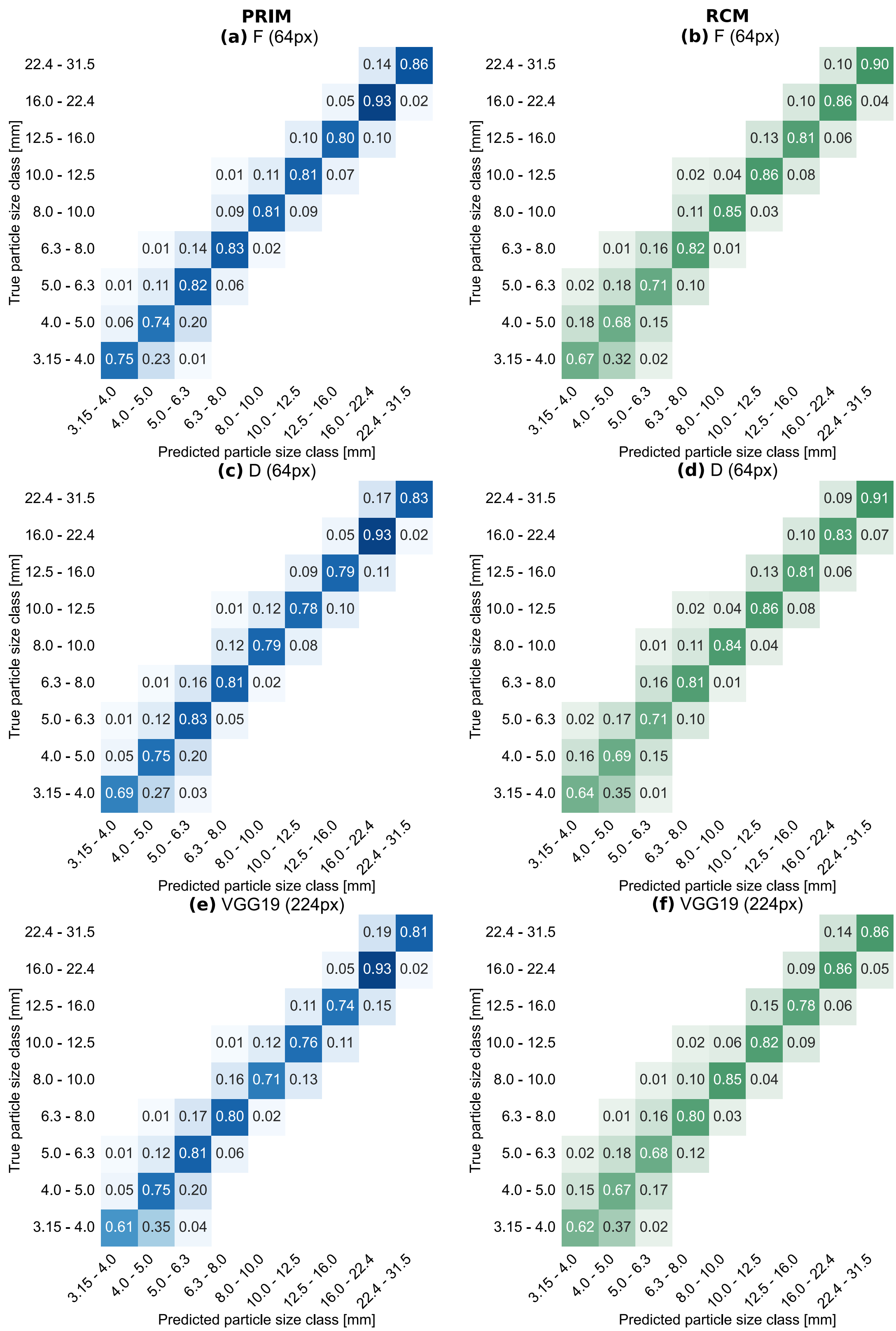

Fig. 4. Model predictions of selected, top-performing CNNs on validation set visualized as confusion matrices.

training (cf. Table 1). A likely explanation for this effect could be the different (absolute) particle size class intervals due to the R10 series of the used screen mesh sizes (cf. Section 2.2). While particle size class interval for the lowest particle size class (3.15 mm to 4.0 mm) is 0.85 mm, it is 9.1 mm for the highest investigated particle size class (22.4 mm to 31.5 mm). Thus, particles among the lower particle size classes are more similar in size and thus may be more difficult to correctly by the CNNs.

3.2. Model explainability (RQ 2)

3.2.1. Feature activation

Fig. 5 shows the feature activations (shown in Fig. 5a.ii and Fig. 5b.ii) for the best performing CNN (CNN F) for randomly selected PRIM and RCM particles (shown in Fig. 5a.i and Fig. 5b.i) across all nine investigated particle size classes. In Fig. 5a.ii and Fig. 5b.ii, it can be seen that the feature activations appear to focus on the particle contour rather than the center of the particles or individual parts of the particle (e.g., highest point). Furthermore, the model seems to not only consider the particle itself but also its negative contour, i.e., the immediate background around the particle. As the feature activations indicate a general interaction of the model with the particle contour, the model overall behaves as expected. However, one should note that not all model interactions can be fully explained due to the black box nature of CNNs. An example is the activation of merely parts of the contours, which occurs for instance for particle size classes 12.5 mm – 16 mm and 22.4 mm - 31.5 mm for the PRIM material class.

3.2.2. Class maps

Fig. 6 provides deeper insights into the classification of individual particles for the best performing model (CNN F) through the use of localized class maps, by juxtaposing model *confidence* (alternative probability) on the y-axis (bottom: high confidence, top: low confidence) against the *farness* (deviation of the particles [3DLT images] from the overall dataset) on the x-axis (left: particles very similar to other particles, right: particles significantly diverging from other particles). The distribution of individual particles from the test set is visualized using a kernel density estimation and each particle size class is visualized in a separated color.

A comparison of the farness distribution of the PRIM (Fig. 6a) and RCM (Fig. 6b) particles shows that the farness of the RCM particles is larger than the farness of the PRIM particles, which corresponds to higher variety and more complex particle shapes shown in Fig. 1. Additionally, comparing the model uncertainty of CNN F a higher uncertainty in predicting the particle size class of RCM particles compared to PRIM particles can be distinguished, which corresponds to the lower validation accuracy in the RCM dataset shown in Table 2 and Fig. 4. Combining both insights validates the hypothesis from Section 3.1.4 that a larger variety in particle shapes (=larger farness) in the RCM dataset results in a more difficult classification task and thus a lower model accuracy.

Comparing the farness distribution among the different particle size classes shows that with the exception of the 8.0 mm – 10.0 mm particle size class of RCM, the farness of the smaller particle size classes is larger than the farness of the larger particle size classes (cf. Section 3.1.4). A potential reason for this observation could be that for small particles, even small changes in the particle contour have a relatively larger influence of the farness, since the black background remains constant and the overall particle size class interval in the smaller particle size classes is smaller. In addition, Fig. 6 shows that smaller particle size classes are classified more uncertain, corresponding to the lower accuracy for smaller particle size classes known from Fig. 4. In total, these findings support the hypothesis that smaller particle size classes are more difficult to classify, likely since (i) already small deviations (e.g., edge effects in 3DLT detection of the particle contour) can have a relatively larger influence on the particle image and (ii) the particle size differences in the smaller particle size classes are absolutely smaller (cf. Section 3.1.4).

Analyzing the misclassified particles (upper half of the respective subplots in Fig. 6) shows that the overall model behavior is plausible. First, the incorrectly classified particles have a larger farness (=further away from original data) compared to the correctly classified particles, thus indicating that the CNN has higher difficulty with classifying so-called *outliers*, i.e., particles that deviate more strongly from the overall dataset. Second, as shown by Fig. 4, the CNN predicts maximum one particle size class off in more than 98 % of the cases and never predicts sizes that are more than two particles sizes away from the true class.

3.3. Aggregation to particle size distributions (RQ 3)

To enable an inline sensor-based monitoring of PSDs (cf. Section 1.1), it is not sufficient to predict individual particle size classes at the

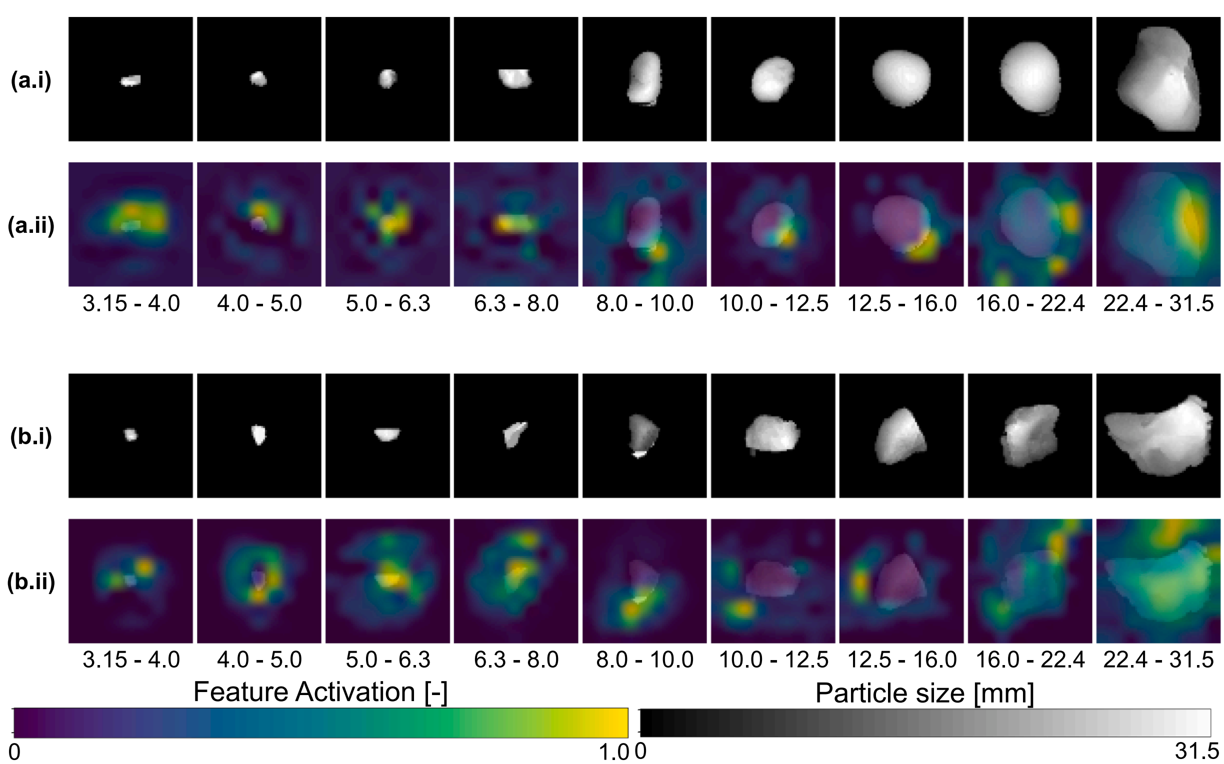

Fig. 5. Feature activations of CNN F for randomly selected PRIM and RCM particles for the nine investigated particle size classed visualized using Grad-CAM.

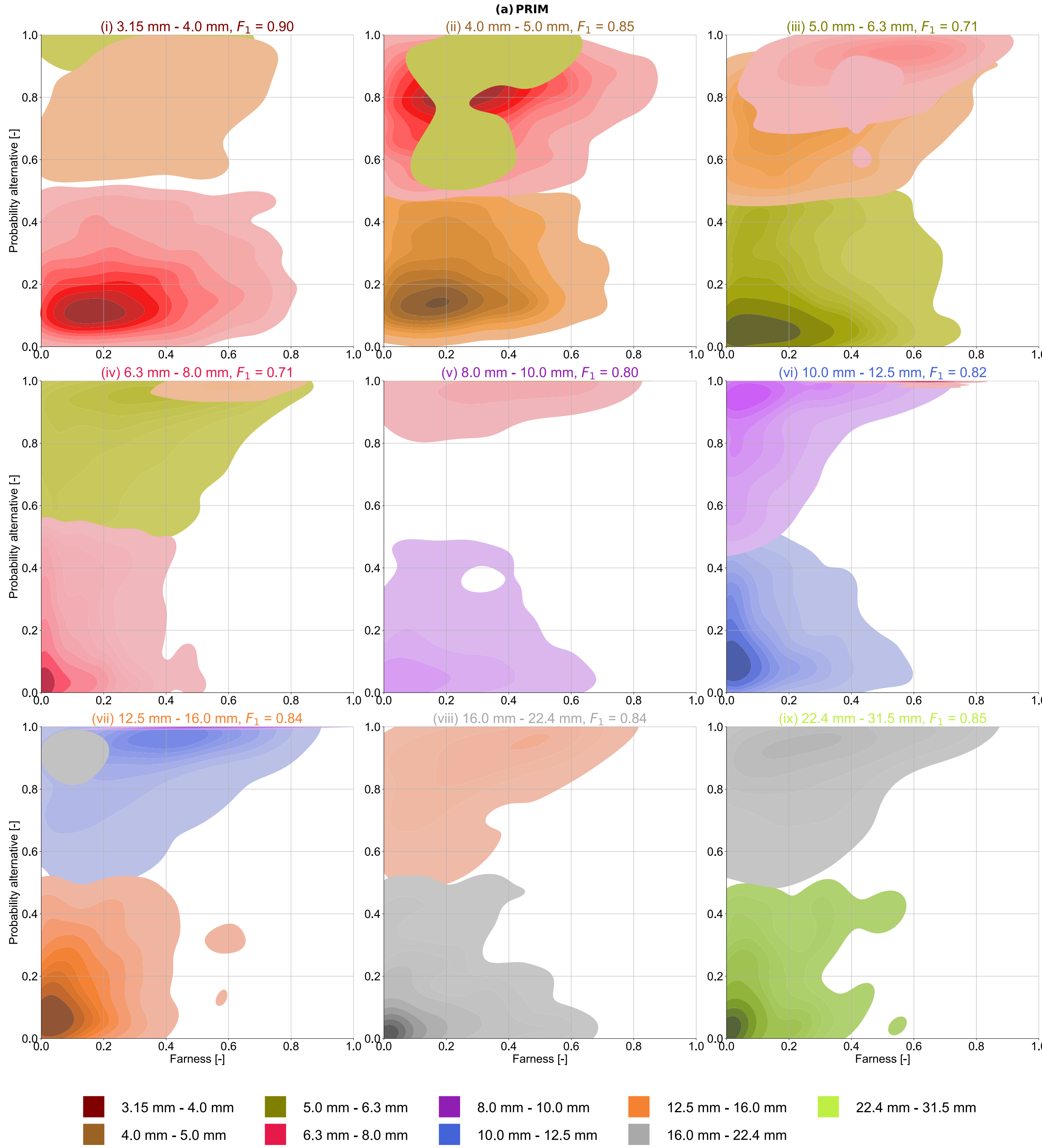

Fig. 6. Class maps for CNN F on the (a) PRIM and (b) RCM dataset across the nine investigated particle size classes. Visualization of density as a kernel-density estimation plot in 10 %-stages, darker colors represent higher densities.

particle level alone, but the predicted particle size classes of thousands of particles have to be aggregated to a PSD at the material flow level, which has the potential advantage that balanced classification errors (one particle size class too low or too high) can even out to some extent.

As such, in Fig. 7, three true and predicted PSDs for the PRIM and RCM particles – based on the independent test set – are compared (cf. Section 2.5.2.1). The true PSDs were derived from the TL SoB-StB 20 [10] norm and correspond to the minimum, maximum, and a mean permissible PSD for the use of RC aggregates in road construction (cf. Table S2).

As shown in Fig. 7, using CNN F, the PSDs can be accurately predicted with a MAE of 1.0 vol% (PRIM: PSD min: 1.2 vol%, PSD mean:

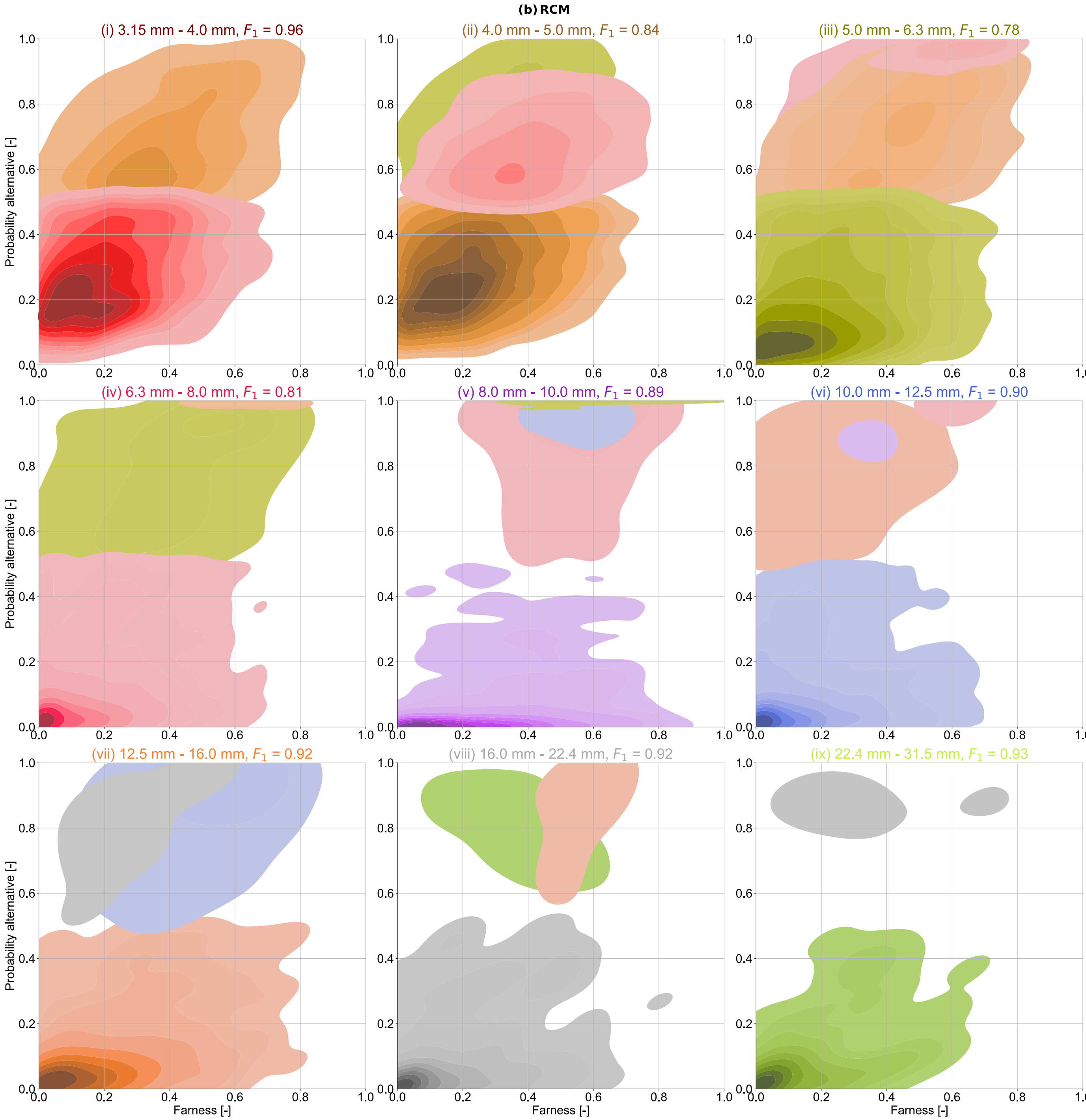

Fig. 6. (*continued*).

0.8 vol%, PSD max: 0.9 vol%; RCM: PSD min: 1.3 vol%, PSD mean: 0.7 vol%, PSD max: 1.0 vol%). Corresponding to the assumption, too large and too small predicted particle size classes are largely evened out, therewith proving the feasibility and robustness of our approach.

3.4. Limitations and future work

As our work focused on investigating the general feasibility of the CNN-based particle size predicting approach, there are several limitations, which should be addressed in future work. First, we investigated only a limited set of deep learning models and optimized only a limited set of hyperparameters over a limited set of settings each. Therefore, investigating additional deep learning models and a more thorough hyperparameter optimization could result in even more accurate predictions. Second, data augmentation and synthetic training data could augment our existing training data to further increase the model performance.

Second, for an industrial application of our results the interference time is of great importance, as the incoming data must be processed in nearly real-time. Therefore, the prediction time of the different models should be compared which each other. These computational time calculations should also consider the necessary segmentation of touching or

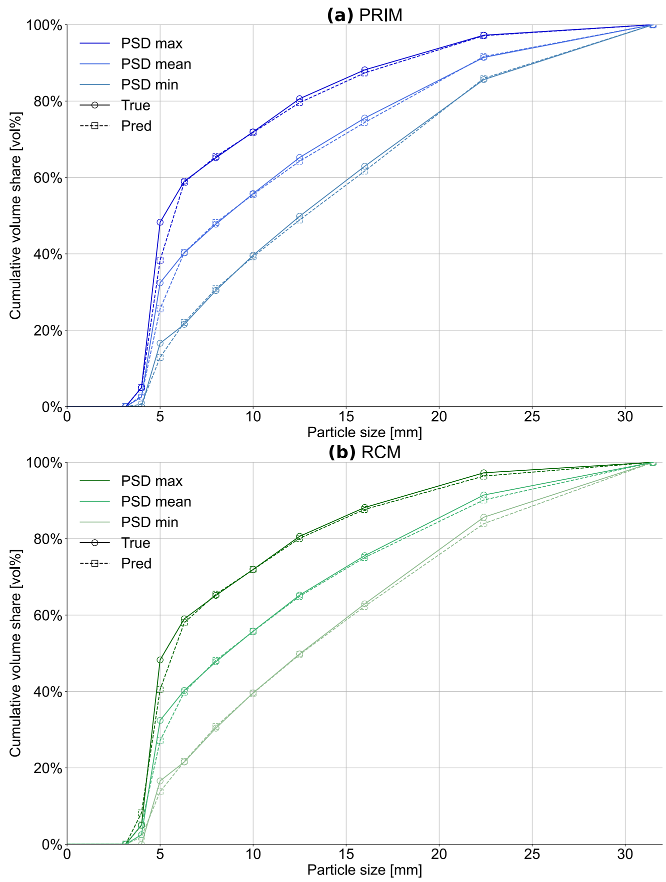

Fig. 7. True and predicted volume-based PSDs based on for the PRIM and RCM dataset using CNN F.

overlapping particles. Therefore, it could also be interesting to investigate the segmentation and particle size prediction end-to-end in a single step (e.g, using semantic instance segmentation).

Third, we compared the PSD prediction only based on 3DLT particle volumes (assuming constant densities), while particle masses are used in ISO 20290-5:2023 [21]. Therefore, the prediction of PSDs should be additionally compared with sieve analysis according to ISO 20290-5:2023 [21], which follows a mass-based weighting of the individual particle classes. Hence, additional prediction errors could occur between the 3DLT-based particle volume to particle mass due to (i) different densities of different materials contained in CDW and (ii) differences between the hull particle volume detected by 3DLT compared to true particle volume (excluding hollow spaces), as is also shown for, e.g., post-consumer lightweight packaging waste [30]. Furthermore, a wide range of investigated PSDs might be of interest to find out which if different PSDs result in different prediction errors or biases.

4. Conclusions

PSDs of recycled aggregates are an essential quality requirement to enable the substitution of primary with RC aggregates in building construction applications and the realization of associated ecological and economic benefits. Currently, PSDs in CDW recycling are determined through sampling and manual sieve analyses, which is time-consuming, costly, and associated with a significant time delay. A promising approach to overcome these limitations of manual PSD determinations is the application of inline sensor technology. Here, we therefore investigated the possibility of predicting PSDs of primary and RC aggregates using 3DLT and CNNs to enable an inline PSD monitoring in CDW recycling plants for an automated quality monitoring and process control.

96,828 and 77,392 particles from primary and RC aggregates, respectively, in the particle size range 3.15 mm to 31.5 mm were sieved, classified into nine particle size classes, and recorded using an inline dual camera 3DLT setup. Based on the created dataset, seven different CNN architectures with different hyperparameter configurations were trained and evaluated.

The custom CNN F architecture showed the highest validation accuracy among all investigated CNN architectures thus indicating a suitable model complexity. No significant changes have been found between transfer learning models trained on 64 px versus 224 px input sizes, indicating that an input image of 64 px is sufficient for the investigated particle size range. Compared to the primary aggregates, predicting the particle size prediction of the RC aggregates is more complex, as shown by a 4.9 percentage points lower validation accuracy across all models and a higher model uncertainty. The top performing CNN F achieved a validation accuracy of 80.8 % for the primary and 75.0 % for the RC aggregates, respectively. 98 % of all classifications occurred within ± one particle size class and no classifications were more than two particle size classes away from the true class. [RQ 1]

The applied XAI methods reveal an overall robust and plausible model behavior. First, an analysis of feature activations using Grad-CAM [37] revealed that the model focuses on particle contour instead of the entire particle area or the highest point on the particle surface. However, not all feature activations could be fully explained due to the black-box-nature of CNNs. Second, class maps confirm that smaller particle size classes are more difficult to be correctly classified by the model, resulting in a higher model uncertainty and lower F_1-score. [RQ 2]

Aggregating the predicted particle size classes of CNN F to PSDs at the material flow level indicates that the PSDs of both primary and RC aggregates are predicted within ± 1.0 vol% MAE. The aggregation at the material flow level shows the advantage that balanced classification errors of individual particles can be largely evened out. [RQ 3]

In future work, our approach should be further validated with mass-based sieve analysis across a large PSD range and additional deep learning techniques could be investigated. In addition, our investigation should be extended to technical lab and industrial scale, where an extension of particle size range, the segmentation of overlapping particles [46], and the correction of segregation effects [28] are remaining challenges that need to be addressed.

Overcoming these challenges and enabling an inline sensor-based monitoring of particle size distributions in CDW recycling promises not only a higher transparency, but also a higher quality of produced RC aggregates based on an inline quality monitoring and adaptive process control. These improved and more transparent qualities can help to further increase the substitution of primary aggregates in building construction applications and can thus support the realization of a more circular and sustainable construction industry.

Funding

This work was funded by the National Austrian Research Promotion Agency (FFG) within the program "Production of the Future" under the project EsKorte (grant no. 877341) and the German Federal Ministry of Education and Research (BMBF) within the program "Digital GreenTech" under the project KIMBA (grant no. 2WDG1693D). Open access funding was provided by the RWTH Aachen University Open Access Publication Fund. The responsibility for the content of this publication lies with the authors.

CRediT authorship contribution statement

Kroell Nils: Writing – review & editing, Writing – original draft, Visualization, Validation, Supervision, Software, Project administration, Methodology, Investigation, Funding acquisition, Formal analysis, Data curation, Conceptualization. **Thor Eric:** Writing – review & editing, Visualization, Validation, Software, Methodology, Formal analysis, Data curation. **Göbbels Lieve:** Writing – review & editing, Visualization, Validation, Software, Methodology, Formal analysis. **Schönfelder Paula:** Writing – review & editing, Validation, Investigation, Data curation. **Chen Xiaozheng:** Writing – review & editing, Methodology, Funding acquisition, Conceptualization.

Declaration of Competing Interest

The authors declare that they have no known competing financial interests or personal relationships that could have appeared to influence the work reported in this paper.

Acknowledgments

We would like to thank MAV Krefeld GmbH for providing the CDW sample material.

Appendix A. Supporting information

Supplementary data associated with this article can be found in the online version at doi:10.1016/j.conbuildmat.2025.140214.

Data availability

The data that has been used is confidential.

References

[1] Bundesverband Baustoffe–Steine und Erden eV. Mineralische Bauabfälle Monitoring 2020: Bericht zum Aufkommen und zum Verbleib mineralischer Bauabfälle im Jahr 2020. Berlin; 2023.
[2] D. Caro, C. Lodato, A. Damgaard, J. Cristóbal, G. Foster, F. Flachenecker, D. Tonini, Environmental and socio-economic effects of construction and demolition waste recycling in the European Union, Sci. Total Environ. 908 (2024) 168295, https://doi.org/10.1016/j.scitotenv.2023.168295.
[3] A. Di Maria, J. Eyckmans, K. van Acker, Downcycling versus recycling of construction and demolition waste: combining LCA and LCC to support sustainable policy making, Waste Manag. (New York, N.Y.) 75 (2018) 3–21, https://doi.org/10.1016/j.wasman.2018.01.028.
[4] G. Dunnu, T. Hilber, U. Schnell, Advanced size measurements and aerodynamic classification of solid recovered fuel particles, Energy Fuels 20 (4) (2006) 1685–1690, https://doi.org/10.1021/ef0600457.
[5] V.A. Epanechnikov, Non-Parametric Estimation of a Multivariate Probability Density, Theory Probab. Appl. 14 (1) (1969) 153–158, https://doi.org/10.1137/1114019.
[6] European Comission, The European Green Deal, Brussels, Belgium, 2019. https://commission.europa.eu/strategy-and-policy/priorities-2019-2024/european-green-deal_en.
[7] European Commission, European Construction Sector Observatory. Improving energy and resource efficiency: Analytical Report, 2018. ⟨https://single-market-economy.ec.europa.eu/document/download/eac86e75-3865-47ea-8411-a9a707da3e05_en⟩.
[8] European Commission, A new Circular Economy Action Plan. Brussels, Belgium; (2020). https://environment.ec.europa.eu/strategy/circular-economy-action-plan_en.
[9] Deutsches Institut für Normung e.V. DIN EN 12620: Gesteinskörnungen für Beton, Verlag, Berlin: Beuth, 2008.
[10] Forschungsgesellschaft für Straßen- und Verkehrswesen, Technische Lieferbedingungen für Baustoffgemische zur Herstellung von Schichten ohne Bindemittel im Straßenbau: TL SoB-StB 20. 2020th ed. Köln, FGSV Verlag GmbH, 2020.
[11] Forschungsgesellschaft für Straßen- und Verkehrswesen. Technische Lieferbedingungen für Gesteinskörnungen im Straßenbau: TL Gestein-StB 04/23, 2004th ed, FGSV Der Verlag, Köln, 2023.
[12] J.-L. Gálvez-Martos, D. Styles, H. Schoenberger, B. Zeschmar-Lahl, Construction and demolition waste best management practice in Europe, Resour. Conserv. Recycl. 136 (2018) 166–178, https://doi.org/10.1016/j.resconrec.2018.04.016.
[13] L. Gao, Y. Yan, G. Lu. On-line measurement of particle size distribution using piezoelectric sensors, IEEE International Instrumentation and Measurement Technology Conference Proceedings; 13.05.2012 - 16.05.2012, IEEE, Graz, Austria, 2012, https://doi.org/10.1109/I2MTC.2012.6229391.
[14] Y. Ge, Z. Lin, H. Tang, P. Zhong, B. Cao, Measurement of particle size of loose accumulation based on alpha shapes (AS) and hill climbing-region growing (HC-RG) algorithms, Sensors (Basel, Switzerland) 20 (3) (2020), https://doi.org/10.3390/s20030883.
[15] He K., Zhang X., Ren S., Sun J. Deep Residual Learning for Image Recognition; 2015.
[16] M. Hinzmann, A. Araujo Sosa, M. Hirschnitz-Garbers, Stärkung der Kreislaufführung von mineralischen Baustoffen mittels freiwilliger Selbstverpflichtung - Akteursperspektiven auf Bedarfe und Optionen: Akteursanalyse im Projekt Ressourcenpolitik, PolRess 2 (2) (2019).
[17] G. Huang, Z. Liu, L. van der Maaten, K.Q. Weinberger. Densely Connected Convolutional Networks, 2016, https://doi.org/10.1109/CVPR.2017.243.
[18] R. Hussain, M. Alican Noyan, G. Woyessa, R.R. Retamal Marín, P. Antonio Martinez, F.M. Mahdi, et al., An ultra-compact particle size analyser using a CMOS image sensor and machine learning, Light Sci. Appl. 9 (2020) 21, https://doi.org/10.1038/s41377-020-0255-6.
[19] International Organization for Standardization ISO/CD 18985. Recycled aggregates for concrete (draft).
[20] International Organization for Standardization ISO/WD TS 21056. Recycled aggregate concrete — Additional provisions and guidance for specification, performance, and production (draft).
[21] International Organization for Standardization ISO 20290-5:2023. Aggregates for concrete — Test methods for mechanical and physical properties Part 5: Determination of particle size distribution by sieving method.
[22] L. Kandlbauer, K. Khodier, D. Ninevski, R. Sarc, Sensor-based particle size determination of shredded mixed commercial waste based on two-dimensional images, Waste Manag. (New York, N.Y.) 120 (2021) 784–794, https://doi.org/10.1016/j.wasman.2020.11.003.
[23] D.P. Kingma, J. Ba, Adam: A method for stochastic optimization, arXiv 2014; 1412.6980 (2014), https://doi.org/10.48550/arXiv.1412.6980.
[24] F. Knappe, J. Reinhardt, A. Schorb, S. Theis, Leitfaden zum Einsatz von, R-Beton (2017). https://um.baden-wuerttemberg.de/fileadmin/redaktion/m-um/intern/Dateien/Dokumente/2_Presse_und_Service/Publikationen/Umwelt/Leitfaden_R-Beton.pdf.
[25] M. Kontny, Machine vision methods for estimation of size distribution of aggregate transported on conveyor belts, Vibroengineering Procedia 13 (2017) 296–300, https://doi.org/10.21595/vp.2017.19151.
[26] N. Kroell, imea: A Python package for extracting 2D and 3D shape measurements from images, JOSS 6 (60) (2021) 3091, https://doi.org/10.21105/joss.03091.
[27] N. Kroell, X. Chen, K. Greiff, A. Feil, Optical sensors and machine learning algorithms in sensor-based material flow characterization for mechanical recycling processes: a systematic literature review, Waste Manag. (New York, N.Y.) 149 (2022) 259–290, https://doi.org/10.1016/j.wasman.2022.05.015.
[28] N. Kroell, X. Chen, B. Küppers, J. Lorenzo, A. Maghmoumi, M. Schlaak, et al., Near-infrared-based determination of mass-based material flow compositions in mechanical recycling of post-consumer plastics: technical feasibility enables novel applications, Resour. Conserv. Recycl. 191 (2023) 106873, https://doi.org/10.1016/j.resconrec.2023.106873.
[29] N. Kroell, X. Chen, B. Küppers, S. Schlögl, A. Feil, K. Greiff, Near-infrared-based quality control of plastic pre-concentrates in lightweight-packaging waste sorting plants, Resour. Conserv. Recycl. 201 (2024) 107256, https://doi.org/10.1016/j.resconrec.2023.107256.
[30] N. Kroell, X. Chen, A. Maghmoumi, M. Koenig, A. Feil, K. Greiff, Sensor-based particle mass prediction of lightweight packaging waste using machine learning algorithms, Waste Manag. (New York, N.Y.) 136 (2021) 253–265, https://doi.org/10.1016/j.wasman.2021.10.017.
[31] N. Kroell, K. Johnen, X. Chen, A. Feil, Fine metal-rich waste stream characterization based on RGB data: Comparison between feature-based and deep learning classification methods, in: J. Beyerer, T. Längle (Eds.), OCM 2021 - Optical Characterization of Materials: Conference Proceedings, KIT Scientific Publishing, 2021.
[32] Kroell N., Schönfelder P., Chen X., Johnen K., Feil A., Greiff K. Sensorbasierte Vorhersage von Korngrößenverteilungen durch Machine Learning Modelle auf Basis von 3D-Lasertriangulationsmessungen. In: Bockreis A, Faulstich M, Flamme S, Kranert M, Mocker M, Nelles M, Quicker P, Rettenberger G, Rotter VS. 11. DGAW-Wissenschaftskongress "Abfall- und Ressourcenwirtschaft": Dresden; 2022b.
[33] Landesamt für Natur, Umwelt und Verbraucherschutz Nordrhein-Westfalen. Verwendung von Beton mit rezyklierter Gesteinskörnung: Kreisläufe im Hochbau schließen, Recklinghausen: Landesamt für Natur, Umwelt und Verbraucherschutz Nordrhein-Westfalen (2021). https://www.lanuv.nrw.de/fileadmin/lanuvpubl/1_infoblaetter/LANUV_Handout_Beton_neu.pdf.
[34] J. Lederer, A. Gassner, F. Kleemann, J. Fellner, Potentials for a circular economy of mineral construction materials and demolition waste in urban areas: a case study from Vienna, Resour. Conserv. Recycl. 161 (2020) 104942, https://doi.org/10.1016/j.resconrec.2020.104942.
[35] J. Moschen-Schimek, T. Kasper, M. Huber-Humer, Critical review of the recovery rates of construction and demolition waste in the European Union - an analysis of influencing factors in selected EU countries, Waste Manag. (New York, N.Y.) 167 (2023) 150–164, https://doi.org/10.1016/j.wasman.2023.05.020.
[36] L. Prechelt, Early Stopping - But When? in: G. Goos, J. Hartmanis, J. van Leeuwen, G.B. Orr, K.-R. Müller (Eds.), Neural Networks: Tricks of the Trade Springer Berlin Heidelberg, Berlin, Heidelberg, 1998, pp. 55–69.
[37] Selvaraju R.R., Cogswell M., Das A., Vedantam R., Parikh D., Batra D. Grad-CAM: Visual Explanations from Deep Networks via Gradient-based Localization 2016. http://doi.org10.48550/arXiv.1610.02391.
[38] I.M. Simion, M.E. Fortuna, A. Bonoli, M. Gavrilescu, Comparing environmental impacts of natural inert and recycled construction and demolition waste processing using LCA, J. Environ. Eng. Landsc. Manag. 21 (4) (2013) 273–287, https://doi.org/10.3846/16486897.2013.852558.

[39] K. Simonyan, A. Zisserman, Very Deep Convolutional Networks for Large-Scale Image, Recognition (2014), https://doi.org/10.48550/arXiv.1409.1556.
[40] K. Tudeshki, Method for Determining the Particle Size Distribution of Granular Material in a Delivery Flow, and Measuring Device (2017). ⟨https://patentscope.wipo.int/search/en/detail.jsf?docId=WO2017055063⟩.
[41] M. Ulucan, K.E. Alyamac, An integrative approach of the use of recycled concrete aggregate in high-rise buildings: example of the Elysium, Struct. Concr. 24 (3) (2023) 3329–3350, https://doi.org/10.1002/suco.202200512.
[42] M. Ulucan, Y. Tas, K.E. Alyamac, Multi-objective optimization and assessment of recycled concrete aggregates for sustainable development: example of the Kömürhan bridge, Struct. Concr. 24 (5) (2023) 5750–5768, https://doi.org/10.1002/suco.202201018.
[43] UN General Assembly, Transforming our world : the 2030 Agenda for Sustainable Development A/RES/70/1 (2015) 21. https://www.un.org/en/development/desa/population/migration/generalassembly/docs/globalcompact/A_RES_70_1_E.pdf.
[44] S. van der Walt, J.L. Schönberger, J. Nunez-Iglesias, F. Boulogne, J.D. Warner, N. Yager, et al., scikit-image: image processing in Python, PeerJ 2 (2014) e453, https://doi.org/10.7717/peerj.453.
[45] B. Wang, L. Yan, Q. Fu, B. Kasal, A comprehensive review on recycled aggregate and recycled aggregate concrete, Resour. Conserv. Recycl. 171 (2021) 105565, https://doi.org/10.1016/j.resconrec.2021.105565.
[46] X. Wu, N. Kroell, K. Greiff, Deep learning-based instance segmentation on 3D laser triangulation data for inline monitoring of particle size distributions in construction and demolition waste recycling, Resour. Conserv. Recycl. 205 (2024) 107541, https://doi.org/10.1016/j.resconrec.2024.107541.
[47] Y. Bengio, Practical recommendations for gradient-based training of deep architectures, 2012, doi:10.48550/arXiv.1206.5533.
[48] Zhang Y., Liang Y. Research on soft-sensor based on support vector regression for particle size of grinding and classification process. In: 2016 Chinese Control and Decision Conference (CCDC); 28.05.2016 - 30.05.2016: Yinchuan, China: IEEE; 2016.